Subsurface oceans and deep interiors of medium-sized outer planet satellites and large trans-neptunian objects

Hauke Hussmann [a,*], Frank Sohl [b], Tilman Spohn [b]

[a] *Instituto de Astronomia, Geofísica e Ciências Atmosféricas (IAG), Universidade de São Paulo (USP), Rua do Matão 1226, Cidade Universitária 05508-900, São Paulo, SP, Brazil*
[b] *German Aerospace Center (DLR), Institute of Planetary Research, Rutherfordstr. 2, D-12489 Berlin, Germany*

Abstract

The detection of induced magnetic fields in the vicinity of the jovian satellites Europa, Ganymede, and Callisto is one of the most surprising findings of the *Galileo* mission to Jupiter. The observed magnetic signature cannot be generated in solid ice or in silicate rock. It rather suggests the existence of electrically conducting reservoirs of liquid water beneath the satellites' outermost icy shells that may contain even more water than all terrestrial oceans combined. The maintenance of liquid water layers is closely related to the internal structure, composition, and thermal state of the corresponding satellite interior. In this study we investigate the possibility of subsurface oceans in the medium-sized icy satellites and the largest trans-neptunian objects (TNO's). Controlling parameters for subsurface ocean formation are the radiogenic heating rate of the silicate component and the effectiveness of the heat transfer to the surface. Furthermore, the melting temperature of ice will be significantly reduced by small amounts of salts and/or incorporated volatiles such as methane and ammonia that are highly abundant in the outer Solar System. Based on the assumption that the satellites are differentiated and using an equilibrium condition between the heat production rate in the rocky cores and the heat loss through the ice shell, we find that subsurface oceans are possible on Rhea, Titania, Oberon, Triton, and Pluto and on the largest TNO's 2003 UB$_{313}$, Sedna, and 2004 DW. Subsurface oceans can even exist if only small amounts of ammonia are available. The liquid subsurface reservoirs are located deeply underneath an ice-I shell of more than 100 km thickness. However, they may be indirectly detectable by their interaction with the surrounding magnetic fields and charged particles and by the magnitude of a satellite's response to tides exerted by the primary. The latter is strongly dependent on the occurrence of a subsurface ocean which provides greater flexibility to a satellite's rigid outer ice shell.
© 2006 Elsevier Inc. All rights reserved.

Keywords: Satellites, general; Trans-neptunian objects; Interiors; Tides, solid body

1. Introduction

The giant planets Jupiter, Saturn, their satellites, rings and magnetospheres have been the main target of two recent planetary orbiter missions aimed at the exploration of the outer Solar System. The *Galileo* mission ended in September 2003 after returning data from the jovian system for almost eight years. In July 2004 the *Cassini* spacecraft arrived at its destiny and will explore the saturnian system in a similar way at least for the duration of the primary mission of about four years. Besides the

planet itself and its rings, a main focus of the mission will be the exploration of the satellite system of Saturn.

One of the most intriguing findings of the *Galileo* mission is the existence of secondary induced magnetic fields in the vicinity of Europa (Khurana et al., 1998; Kivelson et al., 2000), Callisto (Zimmer et al., 2000), and Ganymede (Kivelson et al., 2002). Such fields, which provide strong observational evidence for subsurface oceans in these moons, are generated by ions contained in a liquid water layer underneath the outer icy shells. The induced fields are a result of the interaction of the ions with the magnetic field of Jupiter. The possible existence of liquid water layers in all three icy Galilean satellites raises the question of whether internal oceans are a common feature on icy satellites in general. From theoretical considerations, this

* Corresponding author.
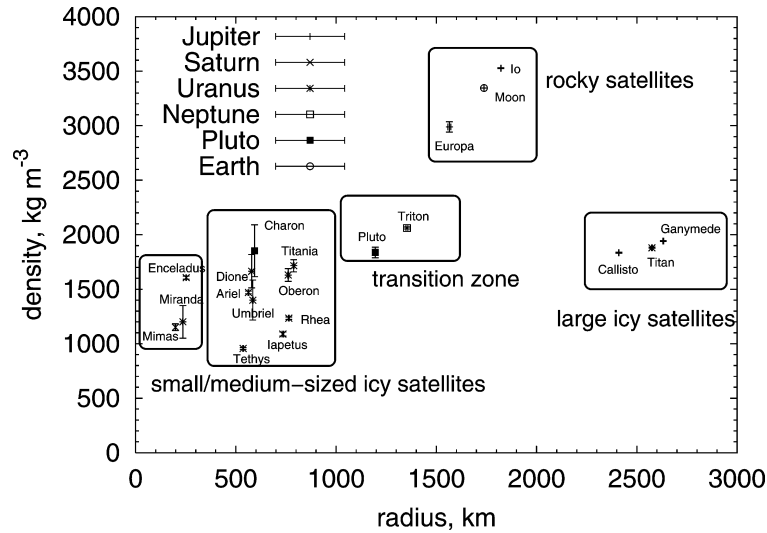 *E-mail address:* hhussman@uni-muenster.de (H. Hussmann).

Fig. 1. Radius–density relation of the natural satellites of the Solar System. It is distinguished between small, medium-sized, transitional, rocky, and large icy satellites. Different symbols represent the respective primary planets. The mean densities of the icy satellites range from about 1000 kg m^{-3} (Tethys) to 2000 kg m^{-3} (Triton). Note that the mean densities of the mid-sized satellites in the saturnian system are lower than those in the uranian, neptunian, and Pluto–Charon system.

was suggested earlier by Lewis (1971) for icy bodies with radii larger than 900 km, e.g., Europa, Ganymede, Callisto, Titan, Triton, and also Pluto.

The relation between radius and density for natural satellites larger than 190 km in radius and the Pluto–Charon system is shown in Fig. 1 using observational data as summarized in Table 1. The mean density of a planetary body is closely related to its bulk composition. Depending on the rock-to-ice ratio, we may distinguish between five groups:

(1) the large icy satellites with low densities, Ganymede, Callisto, and Titan;
(2) the rocky satellites Io, Europa, and the Moon. In spite of its icy surface, Europa rather belongs to the rocky satellites because its bulk metal and silicate content exceeds 90 wt%;
(3) the transition zone occupied by Triton and Pluto and other like-sized Kuiper belt objects indicating a still relatively high rock content;
(4) the medium-sized icy satellites of Saturn and Uranus. The comparatively low densities and spectral signatures indicate that their interiors are mainly composed of water ice;
(5) the small satellites where we did not consider objects smaller than Mimas.

The dominant internal heat sources of planetary satellites are:

(1) radiogenic heating in the silicate component due to the decay of the long-lived radiogenic isotopes uranium, thorium and potassium;
(2) accretional energy as a remnant from the formation process;
(3) energy of differentiation, e.g., the release of gravitational energy during core formation; and
(4) tidal heating.

Table 1
Physical properties of the largest ($R_p > 190$ km) satellites of the outer Solar System and Pluto

	R_p, km	M_p, 10^{20} kg	ρ, kg m^{-3}
Io[1]	1821.6 ± 0.5	893.2 ± 0.1	3527 ± 4
Europa[1]	1565.0 ± 8	480.0 ± 0.1	2989 ± 47
Ganymede[1]	2631.2 ± 1.7	1481.9 ± 0.2	1942 ± 4
Callisto[1]	2410.3 ± 1.5	1075.9 ± 0.1	1834 ± 4
Mimas[2,3]	198.8 ± 1.5	0.379 ± 0.002	1152 ± 32
Enceladus[2,3]	252.3 ± 0.6	1.08 ± 0.002	1606 ± 14
Tethys[2,3]	536.3 ± 1.5	6.18 ± 0.002	956 ± 8
Dione[2,3]	562.5 ± 1.5	10.96 ± 0.002	1470 ± 12
Rhea[2,3]	764.5 ± 2.0	23.10 ± 0.03	1234 ± 11
Titan[2,3]	2575.5 ± 2.0	1345.5 ± 0.18	1880 ± 5
Iapetus[2,3]	734.5 ± 4.0	18.1 ± 0.007	1088 ± 18
Miranda[4,5]	235.8 ± 0.7	0.659 ± 0.075	1201 ± 149
Ariel[4,5]	578.9 ± 0.6	13.53 ± 1.2	1665 ± 153
Umbriel[4,5]	584.7 ± 2.8	11.72 ± 1.4	1400 ± 184
Titania[4,5]	788.9 ± 1.8	35.27 ± 0.9	1715 ± 56
Oberon[4,5]	761.4 ± 2.6	30.14 ± 0.75	1630 ± 58
Triton[6,7]	1353.4 ± 0.9	214.0 ± 0.6	2061 ± 9
Pluto[8,9]	1195.0 ± 5	131.4 ± 1.8	1838 ± 49
Charon[9,10]	603.6 ± 1.4	16.2 ± 0.9	1757 ± 111

Notes. The masses are calculated from the referenced GM_p-values using $G = (6.67259 \pm 0.00085)$ m^3 kg^{-1} s^{-2} (Gillies, 1990) for the constant of gravitation. The mean densities ρ are calculated from $\rho = 3M_p/4\pi R_p^3$ with the given uncertainties in R_p and M_p. The following references were used: [1] Schubert et al. (2004); [2] Jacobson et al. (2005); [3] http://ssd.jpl.nasa.gov/sat_props.html#ref81 (status of 2005-November-30); [4] Jacobson et al. (1992); [5] Thomas (1988); [6] Jacobson et al. (1991); [7] Thomas (2000); [8] Seidelmann et al. (2002); [9] Null and Owen (1996); [10] Sicardy et al. (2006). Proteus ($R_p = 209$ km) is not included in this study because its mass is not well determined, so far.

Accretional heating was only important at the early stages of satellite evolution and should have subsided significantly until today. The total amount of energy released due to early differentiation is estimated to be about 10% of the accretional energy

(Schubert et al., 1986) or even less and is, therefore, negligible compared to the contribution provided by radiogenic heating. In case of synchronous rotation tidal heating is only important for large satellites on eccentric or inclined orbits. This is the case for Io, Europa, and maybe also for Titan, Triton, and the Pluto–Charon system. In fact, Io is the only satellite where the tidal heating rate exceeds the radiogenic heating rate significantly, leading to intense geologic activity and silicate volcanism on this satellite. However, it cannot be ruled out that tidal heating played an important role during earlier evolutionary phases of some satellites. This may well apply to Ganymede, Triton, Enceladus, and to other medium-sized icy satellites of Saturn and Uranus, the surfaces of which have been heavily modified by processes other than impacts (e.g., Peale, 1999). In the absence of significant tidal heating, internal oceans on small icy satellites of the size of Mimas or Enceladus are expected to have solidified early in the history of the Solar System because of relatively high cooling rates caused by the large surface-to-volume ratio of small spherical bodies. Larger moons, however, with considerable H_2O and silicate contents may have harbored internal oceans up to the present time since the silicate components of those satellites were massive enough to generate heat from the decay of long-lived radiogenic isotopes at a rate sufficient to prevent the freeze-out of liquid subsurface reservoirs. Recently, it has been suggested that internal oceans may exist on medium-sized icy satellites as well (England, 2003; Rainey and Stevenson, 2003).

An important factor for the existence of liquid layers is the presence of ammonia or other volatile constituents. Even small amounts of those additional components will reduce the melting temperature of H_2O significantly, making the existence of internal oceans more likely. This was already recognized by Lewis (1971). Recently, the effect has been investigated in more detail mainly in application to Titan (Grasset et al., 2000; Sohl et al., 2003; Grasset and Pargamin, 2005).

In the present study, we calculate thermal and mechanical equilibrium models of the interior structure of medium-sized icy outer planet satellites and large trans-neptunian objects. We investigate under which conditions (e.g., ammonia content) stable two-layer solutions (rocky core and ice shell) or three-layer solutions (rocky core, internal ocean, and ice shell) can be obtained for the individual satellites. Once the interior structure is determined, it is straightforward to calculate the body tide Love numbers which describe the deformation of a planetary body in response to tidal forces exerted by the primary. The determination of tidal Love numbers based on remote sensing observations from orbiting spacecraft may have the potential to indirectly detect internal oceans because they differ by up to one order of magnitude in the presence or absence of liquid subsurface reservoirs. In application to Titan this was investigated by Sohl et al. (1995), Rappaport et al. (1997), and Castillo et al. (2002).

In the following section, we introduce our model approach that permits the simultaneous calculation of a satellite's interior and thermal structure. In Section 3, the resultant two- and three-layer structural models for the icy satellites and the largest trans-neptunian objects are presented. Section 4 summarizes the discussion and conclusions of this study.

2. The model

We start with the model description of conductive and convective heat transport through the ice shell. After that we describe the internal structure models and apply the heat transport models to the icy bodies. We discuss two cases, the two-layer structural model consisting of a rocky core and an ice-I layer and the three-layer structural model, where the H_2O layer is divided into a liquid part (ocean) and an outer solid part. In both cases we search for solutions, where the heat production rate equals the rate of heat loss through the ice shell using the mean density as model constraint. Since the heat production rate is determined by the rock content, this allows us to derive the core size and the thickness of the outer shell(s). Finally, we compute the tidal Love numbers using plausible rheological assumptions for each individual layer. Material parameters that are taken constant for each icy body are summarized in Table 2.

2.1. Heat transport within the ice layer

There are two major ways of heat transport in planetary bodies: thermal conduction and convection. The latter requires the viscosity of the material (mainly ice or rock) to be sufficiently small and the convecting layers to be thick enough to initiate the transport of warm material from the interior to upper parts of the body and, vice versa. For the icy satellites convection takes place in the 'stagnant lid' regime, where the convective motion is confined to the lower, warmer part of the layer that is overlain by a purely conductive lid. First, we consider a purely conductive ice layer.

2.1.1. Thermal conduction
Consider a planet with radius R_p consisting of a rocky core and an ice layer of thickness D. In the case of thermal conduction the rate at which heat is lost through the surface is given

Table 2
Material parameters

Parameter	Value
Ice I layer	
Density ρ_m, kg m^{-3}	1000
Rigidity[1] μ_m, GPa	3.3
Thermal expansivity α, K^{-1}	1.56×10^{-4}
Thermal conductivity k, Wm^{-1} K^{-1}	3.3
Thermal diffusivity κ, m^2 s^{-1}	1.47×10^{-6}
Melting point viscosity[2] η_0, Pa s	10^{13}
Ammonia–water ocean	
Density ρ_w, kg m^{-3}	1000
Rock core	
Density ρ_c, kg m^{-3}	3500
Rigidity μ_c, GPa	50
Present-day radiogenic heat production rate[3], q_{rad}, W kg^{-1}	4.5×10^{-12}

Notes. The following references were used: [1] Sotin et al. (1998); [2] Hunten et al. (1984); [3] Spohn and Schubert (2003).

by

$$Q_s = 4\pi R_p^2 k \frac{T_{bot} - T_s}{D}\left(1 - \frac{D}{R_p}\right), \tag{1}$$

with the corresponding temperature profile as given by (e.g., Turcotte and Schubert, 2001)

$$T(r) = T_s + \frac{T_{bot} - T_s}{1 - R_{bot}/R_p}\left(\frac{R_{bot}}{r} - \frac{R_{bot}}{R_p}\right), \tag{2}$$

where R_{bot} is the radial distance of the base of the ice shell from the planetary center, and r the radial distance of the point to be considered. k is the thermal conductivity of ice-I taken constant at $3.3\,\mathrm{W\,m^{-1}\,K^{-1}}$, T_{bot} is the temperature at the base of the ice shell, and T_s is the surface temperature. $D = R_p - R_{bot}$ is the thickness of the ice layer. Both equations are connected through Fourier's law $q_s(r) = -k(\mathrm{d}T/\mathrm{d}r)$, where q_s is the surface heat flow in units of watts per unit area. Applying Fourier's law and using $q_s(R) = Q_s/4\pi R_p^2$, Eq. (1) follows directly from Eq. (2). For $R_p \gg D$ the factor $1 - D/R$ is unimportant and Eq. (1) reduces to the heat transported through a plane layer, an approximation which is often made for large planets. However, in our application to the mid-sized icy satellites it is necessary to keep that factor.

As a heat source we consider radiogenic heating in the silicate core of the planetary body. If the silicate mass of the planet, M_c, is determined, the radiogenic heating rate Q_{rad} in units of W can be calculated under the assumption of a chondritic composition of the rocky core:

$$Q_{rad} = M_c q_{rad}, \tag{3}$$

where $q_{rad} = 4.5 \times 10^{-12}\,\mathrm{W\,kg^{-1}}$ is taken as the present-day chondritic radiogenic heat production per unit mass (Spohn and Schubert, 2003). If we further assume that the radiogenic heat production is in equilibrium with the heat loss Q_s through the planetary surface, the temperature profile inside the ice layer is determined. In this case the temperature at the base of the ice shell can be obtained from Eq. (1)

$$T_{bot} = T_s + \frac{D Q_{rad}}{4\pi R_p^2 k(1 - D/R_p)}, \tag{4}$$

using the equilibrium condition

$$Q_s = Q_{rad}. \tag{5}$$

2.1.2. Thermal convection

If the temperatures within the ice layer are sufficiently high, convection will set in at a certain ice thickness. In the 'stagnant lid regime' (e.g., Solomatov, 1995) convective motions are restricted to occur in the lower part of the ice layer. Above the convective region is the stagnant lid with thickness D_{stag}, through which heat is transported by conduction only. Substantial changes in viscosity and temperature are confined to occur in the lid, whereas the convective region is at almost constant (adiabatic) temperature with only small viscosity contrasts (Davaille and Jaupart, 1993; Solomatov, 1995; Grasset and Parmentier, 1998). Depending on the viscosity η, the temperature difference across the convective region is given

by $\Delta T \approx |\eta/(\mathrm{d}\eta/\mathrm{d}T)|$. This is based on experimental results from Davaille and Jaupart (1993) and is consistent with numerical experiments performed by Grasset and Parmentier (1998). With an appropriate viscosity law chosen, this translates into a viscosity drop in the convective region of about one order of magnitude from the bottom to the top. In the present study, the ice I layer is assumed to be viscoelastic with a temperature-dependent viscosity. A general flow law for steady state creep of ice at temperatures above about 0.5 times the melting temperature is (e.g., Durham and Stern, 2001)

$$\dot{\epsilon} = A d^{-p} \sigma^n \exp{-(E^* + PV^*)/RT}, \tag{6}$$

where $\dot{\epsilon}$ is the strain rate, P is hydrostatic pressure, d is grain size, σ is differential or deviatoric stress, R is the gas constant, and A, p, n, E^*, and V^* are flow constants related to the dominant creep mechanism. Laboratory-derived flow laws for pure, polycrystalline ice suggest that both dislocation ($n \geqslant 3$) and grain-size-sensitive creep are appropriate flow mechanisms for ice I, whereas dislocation creep is the dominant mechanism for high-pressure ice phases (Weertman, 1983; Durham et al., 1998; Durham and Stern, 2001). However, the dominant flow mechanisms at geologic timescales and low strain rates may be different from those which occur under laboratory conditions where strain rates are likely to be orders of magnitude higher. In particular, grain growth over time in the presence of low stresses suggests that grain-size-sensitive creep may be the dominant mechanism in many planetary applications (McKinnon, 1998; Durham and Stern, 2001). If grain sizes are small enough and convective stresses are generally low, however, stress-independent diffusion creep ($n = 1$) is likely to dominate (Schubert et al., 1986) and the viscosity η can be written as

$$\eta = \frac{\sigma}{2\dot{\epsilon}} = \frac{1}{2A}\exp(Q^*/RT), \tag{7}$$

where $Q^* = E^* + PV^*$ is the activation enthalpy with E^* the activation energy, and V^* the activation volume. The pressure dependence of the activation enthalpy is similar for dislocation creep, diffusion creep, and grain-size-sensitive creep and can be expressed in terms of the pressure dependence of the melting temperature T_m according to $Q^* = lRT_m$, where l is a dimensionless constant in the range of 18–35 (Kirk and Stevenson, 1987). The viscosity of the ice is then calculated in terms of the homologous temperature, the ratio between the temperature T and the melting temperature T_m, according to (e.g., Kirk and Stevenson, 1987)

$$\eta(T) = \eta_0 \exp[l(T_m/T - 1)], \tag{8}$$

where η_0 is melting point viscosity taken at $10^{13}\,\mathrm{Pa\,s}$ and $l = 25$ as suggested by Hunten et al. (1984). This is equivalent to an activation energy for creep of about $60\,\mathrm{kJ\,mol^{-1}}$ at standard pressure and temperature conditions. The pressure distribution inside the outer ice shell and the underlying deep interior is derived from the density profile being consistent with the satellite's mass and radius (see Table 1) and assuming hydrostatic equilibrium.

The viscosity ratio within the convective interior is small, typically one order of magnitude (Grasset and Parmentier, 1998). For this region the parameterization laws derived for the constant viscosity case are applicable (Grasset and Parmentier, 1998; Schubert et al., 2001) and we calculate the heatflow using the relation between Rayleigh- and Nusselt-number as given by, e.g., Schubert et al. (1979). For a viscosity ratio $\gamma = 10$ between bottom $\eta(T_{bot})$ and top $\eta(T_{top})$ of the convective region, we get

$$\eta(T_{top}) = \gamma \eta(T_{bot}) = 10\eta(T_{bot}). \tag{9}$$

Using Eq. (8) and solving for T_{bot} we obtain

$$T_{bot} = \frac{T_m(D)}{T_m(D_{stag})/T_{top} - \ln\gamma/l}. \tag{10}$$

Note that the melting temperature is calculated for different depths (at the base of the ice shell, D, and at the base of the stagnant lid, D_{stag}). The conductive heat loss Q_{stag} through the stagnant lid is, similar to Eq. (1), given by

$$Q_{stag} = 4\pi R_p^2 k \frac{T_{top} - T_s}{D_{stag}} \left(1 - \frac{D_{stag}}{R_p}\right). \tag{11}$$

Equivalent to Eq. (4), the temperature T_{top} can be calculated using the equilibrium condition $Q_{stag} = Q_{rad}$

$$T_{top} = T_s + \frac{D_{stag} Q_{rad}}{4\pi R_p^2 k(1 - D_{stag}/R_p)}. \tag{12}$$

Thus, T_{bot} and T_{top} are both functions of the stagnant lid thickness D_{stag} only. However, for the three unknowns T_{bot}, T_{top}, and D_{stag} an additional equation is required. For that purpose we use the equilibrium condition that the rate of heat loss out of the convective region equals the rate of heat loss through the stagnant lid

$$Q_{conv} = Q_{stag}, \qquad Q_{stag} = Q_{rad}. \tag{13}$$

Q_{conv} is given by

$$Q_{conv} = 4\pi (R_p - D_{stag})^2 k \frac{T_{bot} - T_{top}}{D - D_{stag}} a Ra^\beta, \tag{14}$$

where $a = 0.12$ and $\beta = 0.3$ are dimensionless constants and Ra is the Rayleigh number, given by

$$Ra = \frac{\alpha \rho_m g (T_{bot} - T_{top})(D - D_{stag})^3}{\kappa \eta}. \tag{15}$$

$\alpha = 1.56 \times 10^{-4}$ K^{-1} is the thermal expansion coefficient of ice-I, $\kappa = 1.47 \times 10^{-6}$ m^2 s^{-1} is the thermal diffusivity, $g = GM_p/R_p^2$ is the gravitational acceleration at the surface (G is the gravitational constant), and η is the mean viscosity within the convective region. The latter is calculated from Eq. (8), where the melting temperature T_m is determined at the midpoint of this region, i.e., at the depth $D_{stag} + 0.5(D - D_{stag})$. The mean temperature of the convective region is given by $T = 0.5 (T_{bot} + T_{top})$. Inserting Eqs. (10) and (12) into Eq. (14), the two Eqs. (13) can be solved numerically. As a solution we obtain the thickness D of the ice layer and the thickness D_{stag} of the stagnant lid. If the heat production rate Q_{rad} is known from the

core mass, the thermal profile and the heat flow are completely determined. The efficiency of the convective heat transport will depend on the combination of the parameters involved, namely, a, β, the viscosity ratio γ and the melting-point viscosity η_0. Depending on the geometry and boundary conditions β can take values between 0.25 and 1/3, with the latter being the value derived analytically for convection in plane layers [see, e.g., the discussion in Spohn and Schubert (2003)]. As a reference value we use $\beta = 0.3$. For the prefactor of the Nusselt number we assume $a = 0.12$, corresponding in combination with β to a critical Rayleigh number of 1000 for the onset of convection. The value of a ranges roughly between 0.1 and 0.3 (Schubert et al., 2001). Deschamps and Sotin (2001) derived a different parameterization in application to the large icy satellites, which corresponds to the one used here, if $\beta = 0.263$ and $a = 0.79$ is used (see also Spohn and Schubert, 2003). It is important to note that the heat flow in our model is determined by the rock content and the equilibrium condition (see below). Thus, parameter variations of the convective heat transport have only an influence on the internal temperature distribution and therefore do not significantly affect our results. As we will show below, most of our model applications yield conductive solutions. At least for their present states thermal convection within the icy shells of the mid-sized satellites is of minor importance.

2.2. Internal structure

In the following we relate the thermal model to the interior structure model. The link is provided by the radiogenic heating rate in the rocky core, which is related to both, the density profile and the thermal state of the planetary body. We assume that the bodies are differentiated into a rocky core and an H_2O shell. For differentiated mid-sized icy bodies the internal pressures are low enough for ice-I to be stable throughout the entire shell (see below). The only body considered in this study (note that we do not consider Ganymede, Callisto, and Titan), where the formation of high-pressure ice would be critical is the neptunian satellite Triton. In the following we do not refer to models including high-pressure ice phases.

Depending on the internal temperature and ammonia content, the inner part of the H_2O shell may be liquid. Therefore we consider two kinds of models: (1) a two-layer model, where the body consists of a rocky core and a solid ice shell, and (2) a three-layer model, in which the H_2O shell is further divided into a liquid water layer and a solid ice shell. Using an equilibrium condition between heat production and heat loss we investigate under which conditions solutions with and without a liquid subsurface ocean can be obtained for the mid-sized icy satellites.

2.2.1. Two-layer structural model

Models of planetary interiors suffer from an inherent non-uniqueness since there are usually fewer constraints than unknowns. If the radius R_p, the mean density ρ (or equivalently the total mass M_p), and the mean moment-of-inertia I_p are used as physical constraints for a spherical planetary body, even two-layer interior structure models would have less constraints than

unknowns, i.e., the core density ρ_c (or equivalently the core mass M_c), the core radius R_c, and the mantle density ρ_m. The mean density ρ of a two-layer spherical body is given by

$$\rho R_p^3 = (\rho_c - \rho_m) R_c^3 + \rho_m R_p^3 \tag{16}$$

from which the relative core radius R_c/R_p and core mass fraction M_c/M_p are calculated according to

$$\frac{R_c}{R_p} = \left(\frac{\rho - \rho_m}{\rho_c - \rho_m} \right)^{1/3} \tag{17}$$

and

$$\frac{M_c}{M_p} = \frac{\rho_c}{\rho} \left(\frac{R_c}{R_p} \right)^3 = \frac{\rho_c}{\rho} \frac{(\rho - \rho_m)}{(\rho_c - \rho_m)}, \tag{18}$$

respectively. The dimensionless mean moment-of-inertia factor (MoI) of a two-layer planetary body is given by

$$\text{MoI} = \frac{I_p}{M_p R_p^2} = \frac{2}{5} \left(\frac{\rho_c}{\rho} \left(\frac{R_c}{R_p} \right)^5 + \frac{\rho_m}{\rho} \left(1 - \left(\frac{R_c}{R_p} \right)^5 \right) \right). \tag{19}$$

Upon insertion of Eq. (17), the MoI factor can be expressed in terms of the densities ρ, ρ_m, and ρ_c:

$$\text{MoI} = \frac{2}{5} \left(\frac{(\rho - \rho_m)^{5/3}}{\rho (\rho_c - \rho_m)^{2/3}} + \frac{\rho_m}{\rho} \right). \tag{20}$$

In Fig. 2, we show contours of R_c/R_p, M_c/M_p, and MoI for plausible ranges of silicate core and ice shell densities normalized to the mean density, ρ_c/ρ and ρ_m/ρ, respectively. Here we assume a two-layer body in hydrostatic equilibrium which corresponds to an increase of density with depth equivalent to the requirement $\rho_c \geqslant \rho$ and $0 \leqslant \rho_m \leqslant \rho$.

If assumptions on the core and mantle density are made, the core mass can be calculated from Eq. (18) and linked to the thermal model through Eq. (3) and the equilibrium conditions Eqs. (5) and (13), respectively. In case of an existing two layer solution, the thermal profile and the internal structure of the body are completely determined. Fig. 3 shows the temperature at the bottom of the ice shell T_{bot} as a function of the surface radius (solid curve), where the mean density of 1240 kg m^{-3} and a surface temperature of 80 K are assumed as an example. Because of the underlying constant-density assumption, an increase in radius corresponds to an increase in the intrinsic heat production, which ranges roughly between 2×10^8 and 1×10^{10} W. From the hydrostatic equation the pressure can be calculated as a function of depth. Using the parameterization of Chizhov (1993), the melting temperature of ice-I at the base of the ice shell (short-dashed line in Fig. 3)

$$T_m = 273.15 \, \text{K} \left(1 - \frac{P}{395.2 \, \text{MPa}} \right)^{1/9} \tag{21}$$

can be calculated from the hydrostatic pressure P. Purely conductive two-layer solutions are only obtained for temperatures at the base of the ice shell below the melting temperature. For satellites with the assumed mean density and radii above 950 km, a subsurface ocean is expected to form between the ice-I layer and the rocky core.
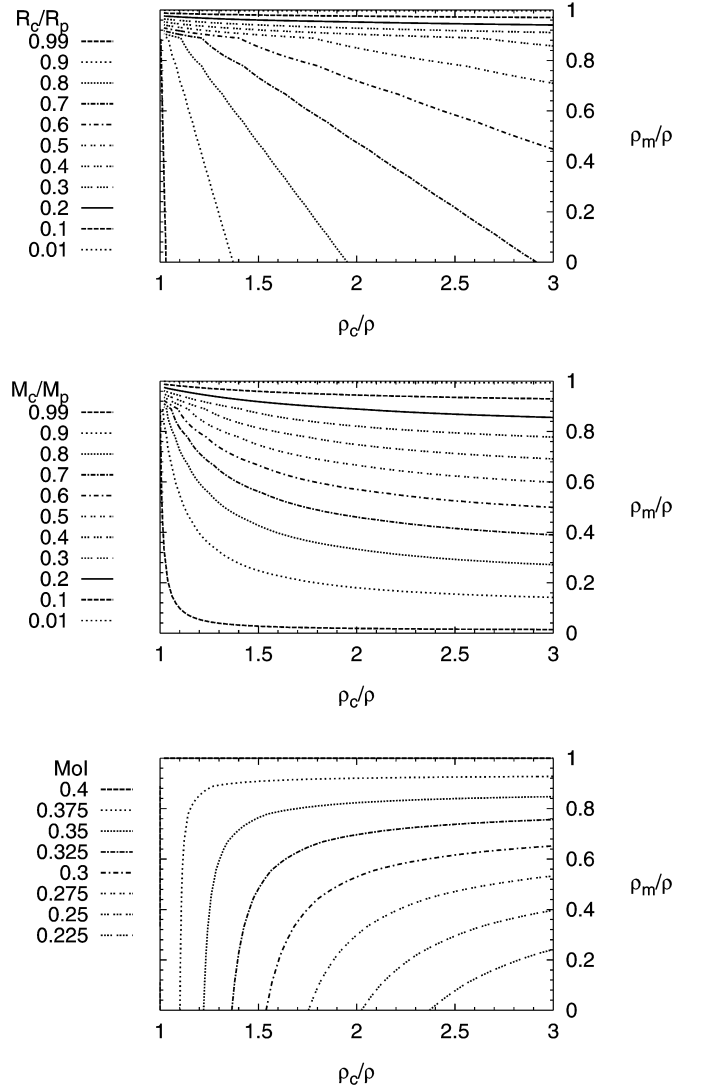

Fig. 2. Contours of (top) relative core radius, R_c/R_p; (middle) relative core mass fraction M_c/M_p; (bottom) mean moment-of-inertia factor, MoI, for two-layer structural models as a function of the ratio of core and mantle density ρ_c and ρ_m, respectively, to mean density ρ.

In the example shown in Fig. 3, the ice layer becomes unstable to convection for satellites larger than 830 km in radius. For radii between 830 and 950 km, both convective and conductive states of the ice layer are possible. Low basal temperatures are then sufficient in case of highly efficient heat transfer by thermal convection. If heat transfer across the ice layer is entirely by conduction, however, higher temperatures are required at the base of the layer to balance surface heat flow and internal heat production. As a consequence, higher basal temperatures could initiate thermal convection, so that the heat loss would exceed internal heat production thereby reducing the bottom temperature due to more efficient cooling.

2.2.2. Models including subsurface oceans

In the following, we consider a satellite that consists of a rocky core, an overlying liquid layer, and an outer ice-I shell. Using general mass balance constraints, we calculate the mass inside the ice-I shell and the pressure at the base of the ice shell
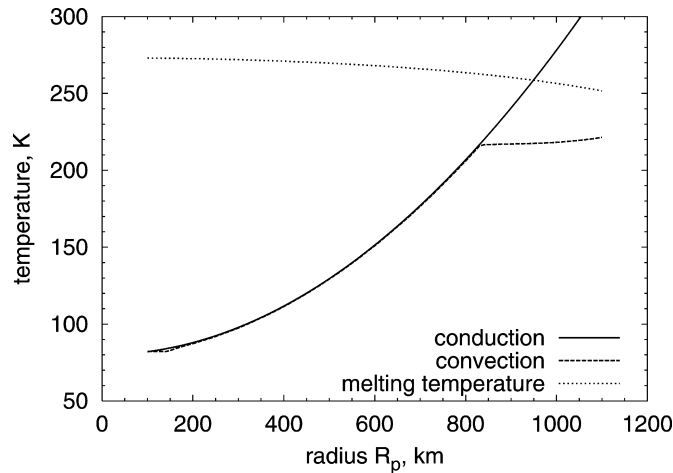
Fig. 3. Ice-I melting temperature and temperature at the base of the ice shell under the assumption of thermal equilibrium. The mean density taken as $1237\ \mathrm{kg\,m^{-3}}$ represents that of Rhea. The solid line shows the basal temperature in case of a purely conducting layer. At about $R_p = 830$ km the ice layer becomes unstable against convection. The long-dashed line shows the basal temperature in the convective case. The conductive profile intersects the melting curve at $R_p \approx 950$ km. For larger satellites subsurface oceans are possible in case of purely conductive heat transport. However, in case of convection, the basal temperature is lower than the melting temperature.

as a function of its thickness, $P = P(D)$. It is straightforward to determine the ice shell thickness D by taking into account the pressure dependence of the melting curve. For that purpose, we use the empirical formula of Chizhov (1993) to calculate the melting temperatures of pure H_2O, whereas polynomial representations reported by Leliwa-Kopystyński et al. (2002) have been evaluated to construct the melting curves for ammonia–water mixtures as a function of pressure and ammonia-content within the subsurface ocean. For a general description of the influence of ammonia on the melting temperature of water–ice; see also Grasset and Pargamin (2005). For an H_2O-layer with constant thickness, the NH_3 content $X = M_{NH_3}/M_{ocean}$ within the liquid will depend on the ice thickness. We assume that the ice layer is made of pure H_2O–ice and we do not distinguish in density between solid ice and the liquid layer. With an initial ammonia concentration of $X_0 = M_{NH_3}/M_{H_2O}$, we obtain $X_0/X = M_{ocean}/M_{H_2O}$. The ice thickness D, which is a function of the NH_3-concentration within the ocean, is then given by

$$D = R_p - \left[X_0\left(R_p^3 - R_c^3\right)/X + R_c^3 \right]^{1/3}. \qquad (22)$$

Since we do not distinguish between the density of solid ice and that of the liquid layer, the core radius can be calculated from the mass balance equation $M_p = M_c + M_{H_2O}$, where M_c is the mass of the rocky core and M_{H_2O} the mass of the entire H_2O-layer consisting of the liquid part and the solid ice-layer

$$R_c = \left(\frac{3M_p/(4\pi) - \rho_m R_p^3}{\rho_c - \rho_m} \right)^{1/3}. \qquad (23)$$

ρ_m is the density of the H_2O-layer. In case of a purely conductive ice-I layer [Eq. (1)] and using again the equilibrium condition $Q_{rad} = Q_s$, the core radius can be written as a func-

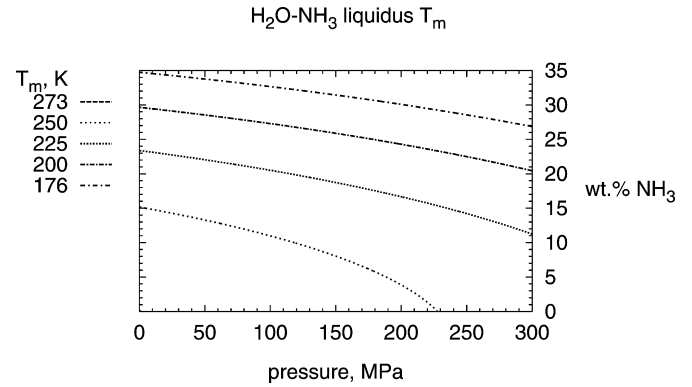Fig. 4. Contours of the melting temperature as a function of ammonia concentration and pressure for an H_2O–NH_3 mixture, according to Eq. (25).

tion of ice thickness D,

$$R_c = R_c(D) = \left(\frac{3R_p^2 k[T_m(P_{base}, X) - T_s](1 - D/R_p)}{\rho_c q_{rad} D} \right)^{1/3}, \qquad (24)$$

where T_m is the melting temperature, set equal to the temperature at the base of the ice shell. In thermal equilibrium, the ocean temperature will increase adiabatically with depth. However, for the pressure range to be expected for the interiors of medium-sized icy satellites the adiabatic temperature increase with ocean depth can be safely neglected. The internal ocean is therefore assumed to be isothermal. Using the experimental data of Leliwa-Kopystyński et al. (2002), the melting temperature, which is a function of pressure P and of the NH_3-concentration within the ocean, is given by

$$T_m(P, X) = c_0 - c_1 P - c_2 P^2 - c_3 X - c_4 X^2 - c_5 P X, \qquad (25)$$

with $c_0 = 273.1$ K, $c_1 = 7.95 \times 10^{-8}$ K Pa^{-1}, $c_2 = 9.6 \times 10^{-17}$ K Pa^{-2}, $c_3 = 0.538 \times 10^2$ K, $c_4 = 6.5 \times 10^2$ K, $c_5 = 4.4 \times 10^{-8}$ K Pa^{-1}, and X is given as the mass ratio M_{NH_3}/M_{ocean}. According to Eq. (25), contours of the melting temperature are shown as a function of pressure and ammonia concentration in Fig. 4. Following Eq. (22) the ice thickness is given as a function of X, and therefore the pressure and consequently the melting temperature T_m are functions of X only. Inserting Eq. (25) into Eq. (24) and equating the latter with Eq. (23), the NH_3 concentration and the thickness of the ice layer at which the thermal equilibrium is established can be calculated. In this case the interior structure, the temperature profile, and the NH_3-concentration within the ocean are completely determined. Since we use the same density for the ice and the liquid water layer, we can still use Eq. (20) to calculate the moment of inertia factor.

The procedure in case of convection is analogous to the two-layer case: an additional layer D_{stag} and an additional equilibrium condition $Q_{stag} = Q_s$ has to be used. We use the same definitions for the Rayleigh and the Nusselt numbers as above. Note that if the subsurface ocean is enriched in ammonia, the viscosity at the base of the ice-I layer is much higher than in the presence of a pure water layer because water–ammonia ocean temperatures are substantially lower (see also Sohl et al., 2003; Tobie et al., 2005).

Equation (25) can only be used for temperatures exceeding the peritectic temperature of the ammonia–water mixture of about 176 K. This corresponds to an NH_3-concentration within the ocean of about 33%. At this point, the water–ammonia layer will crystallize and the temperature within the ocean will stay at the peritectic temperature until it is entirely solidified. Our model is not capable of describing such a scenario including solid ammonia phases. Whenever the peritectic temperature is reached in the calculations we cannot decide if there still exists a liquid part of the ammonia–water mixture or if it is entirely solid at present. In this case we simply state that the peritectic temperature is reached.

2.3. Love numbers

The tidal deformation of a satellite can be obtained from spacecraft measurements. Since it will be indicative of an internal ocean, we calculate the dimensionless complex body tide Love numbers h_2, k_2, and l_2 that measure the tidally-induced radial displacement, radial potential perturbation due to internal mass displacement, and horizontal displacement at the surface of each satellite, respectively. The body tide Love numbers are dependent on the interior structure, rheological properties, and tidal forcing periods and are obtained by numerical integration of the linearized field equations for small viscoelastic deformations in a spherical and self-gravitating body subject to certain boundary and continuity conditions (Segatz et al., 1988; Wieczerkowski, 1999). The correspondence principle (e.g., Zschau, 1978) which relates the viscoelastic problem to the well-known elastic problem permits solving the resultant set of twelve differential equations for the complex radial functions $h_2(r)$, $k_2(r)$, and $l_2(r)$ in the frequency domain. For simplicity, we assume the linear viscoelastic Maxwell rheological model. The real and imaginary parts of the complex rigidity $\tilde{\mu}_i = \text{Re}(\tilde{\mu}_i) + i\,\text{Im}(\tilde{\mu}_i)$ can then be written as

$$\text{Re}(\tilde{\mu}_i) = \frac{\eta_i^2 \omega^2 \mu_i}{\mu_i^2 + \eta_i^2 \omega^2}, \tag{26}$$

$$\text{Im}(\tilde{\mu}_i) = \frac{\eta_i \omega \mu_i^2}{\mu_i^2 + \eta_i^2 \omega^2}, \tag{27}$$

where the tidal forcing frequency ω equals the mean motion of a synchronously rotating satellite n; μ_i and η_i are the elastic rigidity and the steady-state viscosity of the ith layer, respectively. The specific dissipation function of each layer Q_i is then given by

$$Q_i = \frac{\text{Re}(\tilde{\mu}_i)}{\text{Im}(\tilde{\mu}_i)} = n\tau_i, \tag{28}$$

where the Maxwell time $\tau_i = \eta_i/\mu_i$ represents a characteristic timescale distinguishing viscous-like deformation of the ith layer for tidal forcing periods longward of τ_i from its elastic behavior for tidal forcing periods shortward of τ_i. The silicate core is taken to be elastic with a rigidity μ_c of 50 GPa. The subsurface ocean is included as a liquid layer with vanishing rigidity. Tidally-induced deformations of the ice shell are found to be much stronger in the presence of an internal liquid layer.

In case of conduction we divide the ice shell in five different sublayers with the viscosity depending on the mean temperature of a sublayer according to Eq. (8). The temperature of each of the five sublayers is calculated as the arithmetic mean of the two temperatures at the bottom and the top of the sublayer from the conductive temperature profile using Eq. (2). In case of convection, we use the mean viscosity within the convective region and divide the stagnant lid into five sublayers. The shear modulus of ice I, $\mu_m = 3.3 \times 10^9$ Pa (Sotin et al., 1998), is assumed to be constant throughout the calculations.

3. Results

First, we show the solutions obtained for the two-layer structural models in Section 3.1 and for the three-layer models in Section 3.2. In Section 3.3 we apply the three-layer model to the largest known trans-neptunian objects.

3.1. Two-layer structural models

The results for the two-layer model including a rocky core and an ice-I layer are summarized in Table 3 (internal structure), Table 4 (thermal quantities), and Table 5 (tidal Love numbers). The surface temperatures used in the calculations are 100 K for the jovian system, 80 K for the saturnian system, 70 K for the uranian system, and 40 K for the Pluto–Charon system. We assume rock and ice densities of 3500 and 1000 kg m^{-3}, respectively. Two-layer solutions are obtained for all the planetary bodies discussed in this study, except for Triton. The pressure at the bottom of Triton's ice layer is sufficiently high for pressure-induced phase transitions to occur but those will not be further considered in the present study. In case of Europa, the pressure at the base of the relatively thin

Table 3
Results from the 2-layer model

	D, km	R_c, km	R_c/R_p	M_c/M_p	MoI	P_{cmb}, GPa	P_c, GPa
Europa	160.0	1405.0	0.90	0.92	0.346	0.205	4.15
Mimas	120.7	78.1	0.39	0.18	0.355	0.00726	0.0177
Enceladus	95.0	157.3	0.62	0.53	0.308	0.0119	0.0543
Tethys	501.0	29.0	0.06	0.0006	0.399	0.0395	0.0409
Dione	240.2	322.3	0.57	0.45	0.314	0.0607	0.238
Rhea	417.3	347.2	0.45	0.27	0.340	0.111	0.317
Iapetus	491.6	242.9	0.33	0.12	0.370	0.0948	0.196
Miranda	134.2	101.6	0.43	0.23	0.346	0.0104	0.0281
Ariel	206.6	372.3	0.64	0.56	0.306	0.0620	0.299
Umbriel	267.4	317.3	0.54	0.40	0.319	0.0659	0.238
Titania	269.1	519.8	0.66	0.58	0.306	0.114	0.576
Oberon	280.5	480.9	0.63	0.54	0.307	0.108	0.504
Charon	180.0	405.6	0.67	0.60	0.305	0.0656	0.347
Pluto	282.1	854.9	0.75	0.72	0.310	0.205	1.46

Notes. Shown are the thickness of the ice shell, the core radius, the relative core radius, the rock-to-ice mass ratio, the dimensionless axial moment of inertia, the pressure at the core-ice boundary, and the central pressure. Triton is the only body we considered, for which we did not obtain a two-layer solution. For Pluto we used a radius of 1137 km (Yoder, 1995). However, for the value of 1195 km given by Seidelmann et al. (2002), we do not obtain a two-layer solution.

Table 4
Heatflow and temperature at the base of the ice shell obtained from the 2-layer model according to the structure given in Table 3

	Q_s, GW	q_s, mW m^{-2}	T_{bot}, K	Nu
Europa	198	6.4	255	22
Mimas	0.0314	0.063	86	1
Enceladus	0.256	0.321	95	1
Tethys	0.00161	0.00046	81	1
Dione	2.20	0.56	151	1
Rhea	2.76	0.38	185	1
Iapetus	0.946	0.14	143	1
Miranda	0.0692	0.099	79	1
Ariel	3.40	0.81	149	1
Umbriel	2.11	0.50	143	1
Titania	9.26	1.2	217	1
Oberon	7.36	0.10	205	1
Charon	4.40	0.96	126	1
Pluto	41.2	2.5	233	9.8

Note. The Nusselt number Nu indicates whether a conductive ($Nu = 1$) or a convective ($Nu > 1$) solution is obtained.

Table 5
Tidal Love numbers obtained from the 2-layer models according to the internal structures given in Table 3 and the rheology assumptions described in the text

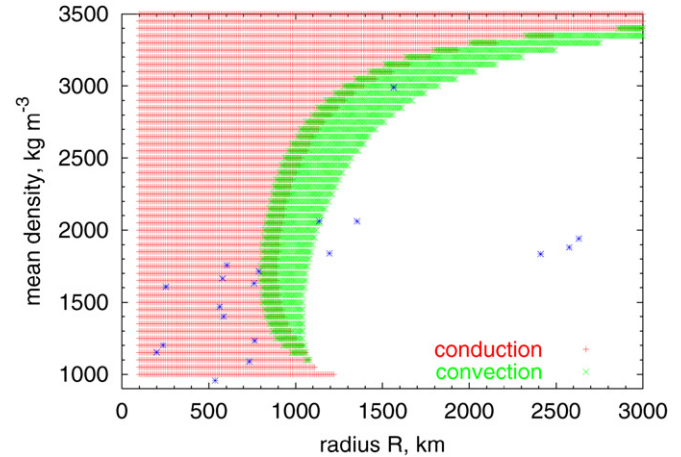|	k_2	h_2	l_2
Europa	0.01857	0.03473	0.01574
Mimas	0.00038	0.00072	0.00028
Enceladus	0.00034	0.00082	0.00045
Tethys	0.00372	0.00620	0.00186
Dione	0.00192	0.00441	0.00226
Rhea	0.00482	0.00976	0.00411
Iapetus	0.00578	0.01047	0.00369
Miranda	0.00049	0.00096	0.00039
Ariel	0.00172	0.00415	0.00234
Umbriel	0.00225	0.00501	0.00244
Titania	0.00310	0.00750	0.00428
Oberon	0.00305	0.00731	0.00406
Charon	0.00177	0.00430	0.00248
Pluto	0.00615	0.01441	0.00848

Fig. 5. The mean density as a function of the radius for the two-layer case. Conductive solutions are located in the red region on the left; convective solutions are obtained in the green region. There is an overlapping region, where both modes of heat transport are possible. Which one is obtained depends on the internal temperatures. On the right from the convective region no two-layer solutions are obtained because the internal pressure requires the formation of high-pressure ices. The icy satellites of the outer Solar System and Pluto are indicated by asterisks. From left to right with increasing radius: Mimas, Miranda, Enceladus, Tethys, Dione, Ariel, Umbriel, Charon, Iapetus, Oberon, Rhea, Titania, Pluto (1137, 1195 km), Triton, Europa, Callisto, Titan, and Ganymede. For Pluto we considered two estimates of its radius (see, e.g., Yoder, 1995).

mass fraction, and the values of the moment of inertia are very similar. In the saturnian system there is no such alignment, and the accretional processes may have been very different for the individual satellites. It is remarkable that the saturnian satellite Tethys is very close to a homogeneous composition of water ice. It has the lowest density of all the bodies considered suggesting a very low rock component. For this body our model is only applicable for low ice densities and very low rock content. In this case the assumption of differentiation may be questionable and an approach assuming a homogeneous mixture would be more appropriate (see, e.g., Multhaup and Spohn, 2005).

Fig. 5 shows the conductive and convective solutions in the R_p, ρ-space for the two-layer case. On the right-hand side, no two-layer solutions are obtained, because the pressure at the base of the ice shell would exceed the critical pressure required for the ice-I–III phase transition to occur. Since we limit ourselves to medium-sized icy satellites, we do not consider this part of the diagram in the present study.

Convective solutions are obtained for satellites where the ice layers are thick and warm enough because of the heating from the silicate core underneath. There is an overlapping region where both convective and conductive solutions are possible. The latter require higher bottom temperatures at the same rate of heat loss (see also Fig. 3). There are two extremes for the interior structure of large bodies shown in Fig. 5. One with high density, with the mean density being close to the rock density (upper right corner) and one with low density, with the mean density being close to the density of ice-I. In the first case, the planetary body consists of a large rocky core and a thin ice layer. The equilibrium is characterized by a large heat flow through the thin ice layer. This explains the curvature at the top of the figures (toward high densities). Larger bodies have

ice shell is sufficiently low to permit two-layer interior models. However, to satisfy the satellite's moment-of-inertia factor of 0.346 (Anderson et al., 1998) it is required to enhance the density contrast between the ice layer and the rock core beyond that used for the other satellites by attaching rock and ice densities of 3780 and 920 kg m^{-3}, respectively. The large rock density value suggests that a Europan silicate core is enriched in heavier elements such as iron or that Europa additionally harbors a dense Fe–FeS core (Anderson et al., 1998; Sohl et al., 2002).

Purely conductive solutions are not obtained for Pluto and Europa so that their outer ice layers are convecting, as indicated by Nusselt numbers $Nu > 1$ in Table 4. This suggests that the internal dynamics of Pluto and Charon, with the ice-layer of the latter being purely conductive would be different. Note that the interior structures of the uranian satellites are similar to those obtained for the Pluto–Charon system. Apart from Miranda, which is significantly smaller than the others, the silicate

larger cores, higher heat production rates, and thinner ice layers. In such a regime, an increase in radius requires an increase in density as well. The mean density is approximating the core density. In the second case, the body has a small rocky core and a thick ice layer (lower part in the figure). Equilibrium is attained for a low heat flux through a thick ice shell. This explains the curvature to the right at low densities. In this case larger bodies have smaller cores, lower heat production rates, but thicker ice layers. In such a regime an increase in radius requires a decrease in mean density with the latter approximating the ice density.

The right border of the convective regime is simply determined by the constraint that no high-pressure ices form. It is therefore independent of other parameters, e.g., the surface temperature used. However, the left border of the convective regime depends to some extent on the parameters chosen. For the construction of Fig. 5, a surface temperature of 70 K is used. The general form of the figure is not changed if other values between 40 K (Pluto–Charon system) and 100 K (Galilean satellites) are used. For higher surface temperatures the convective region extends more to the left. However, a convective solution for Titania and Oberon can only be obtained for 100 K, which is unrealistic for the uranian system. All other satellites stay in the conductive region even if higher surface temperatures are used. For 40 K, Pluto (with an assumed radius of 1137 km) still lies well in the convective region (see also Table 4).

The same holds for other parameters, e.g., thermal conductivity, or the rheology and heat flow parameters, variations of which do not affect the results shown in Fig. 5 significantly. The only quantity, which has a large impact on the extension of the convective region is the radiogenic heating rate. If we raise it by a factor of 2 we find convective solutions also for the largest of the mid-sized satellites. By further increasing this value even the small satellites are located at the boundary of the convective region. This indicates the importance of convection in the satellites' past evolution, when the radiogenic heating rate was significantly higher.

Comparing the silicate mass fraction of the bodies, it is interesting to note that it tends to increase if we go from the saturnian system to the uranian system and further out to Triton and the Pluto–Charon system. It indicates that the bodies of the Kuiper belt may contain a substantial amount of rocks ($>60\%$). The small and medium-sized satellites are found to contain less than 60% silicates. In general, the two-layer model may serve as a valid approximation for the smaller satellites (left bottom corner in Figs. 1 and 5).

3.2. Models including subsurface oceans

The results for models including a rocky core, a subsurface ocean (assumed density 1000 kg m^{-3}), and an ice-I layer are shown in Table 6 (internal structure) and Table 7 (thermal quantities and Love numbers). Examples of some of the solutions are also shown in Figs. 6 and 7. Since it is assumed that there is no density contrast between the ice layer and the liquid layer beneath, the internal structures and the heat flows of the satellites

Table 6
Results from the 3-layer model (ice thickness D, ocean thickness D_{oc}, core radius, relative core radius, rock-to-ice mass ratio, dimensionless axial moment of inertia, ammonia content within the ocean X, assumed initial ammonia content X_0)

	D, km	D_{oc}, km	R_c, km	R_c/R_p	M_c/M_p	MoI	X, %	X_0, %
Europa	79.5	80.5	1405.0	0.90	0.92	0.346	2.1	1.0
	77.5	82.5	1405.0	0.90	0.92	0.346	6.1	3.0
	74.8	85.2	1405.0	0.90	0.92	0.346	9.9	5.0
	70.0	90.0	1405.0	0.90	0.92	0.346	14.9	8.0
	57.0	103.0	1405.0	0.90	0.92	0.346	24.2	15.0
Rhea	400.9	16.4	347.2	0.45	0.27	0.340	32.5	0.5
Titania	253.1	16.0	519.8	0.66	0.58	0.306	26.2	1.0
	229.7	39.4	519.8	0.66	0.58	0.306	30.6	3.0
	217.7	51.5	519.8	0.66	0.58	0.306	32.5	4.3
Oberon	264.4	16.0	481.0	0.63	0.54	0.307	28.7	1.0
	241.1	39.3	481.0	0.63	0.54	0.307	32.5	2.9
Triton	200.5	135.9	1017.0	0.75	0.72	0.310	3.0	1.0
	194.9	141.5	1017.0	0.75	0.72	0.310	8.5	3.0
	187.5	148.9	1017.0	0.75	0.72	0.310	13.4	5.0
	174.8	161.6	1017.0	0.75	0.72	0.310	19.5	8.0
	143.9	192.5	1017.0	0.75	0.72	0.310	29.8	15.0
Pluto	260.6	104.2	830.2	0.70	0.64	0.306	4.7	1.0
	248.7	116.1	830.2	0.70	0.64	0.306	12.4	3.0
	234.9	129.9	830.2	0.70	0.64	0.306	18.1	5.0
	214.5	150.3	830.2	0.70	0.64	0.306	24.5	8.0
	179.9	184.9	830.2	0.70	0.64	0.306	32.5	13.6

Notes. We considered X_0-values of 1, 3, 5, 8, and 15%. In cases where the peritectic composition of 32.5% within the ocean is reached for initial values smaller than 15%, we determined the initial concentration, for which a liquid layer close to the peritectic composition exists (e.g., $X_0 = 13.6\%$ for Pluto or 0.5% for Rhea). In such cases larger initial concentrations will lead to crystallization of solid ammonia compounds. We did not obtain solutions for the remaining satellites (note that we excluded the large icy satellites, Ganymede, Callisto, and Titan).

are identical to those obtained for the two-layer structural models.

We have considered pure water layers, as well as water layers including ammonia. Ammonia reduces the melting temperature of ice and oceans are therefore more likely. Indeed, we did not obtain a single solution in the pure-water case. However, if ammonia is included, solutions with subsurface oceans are obtained. Starting with the smallest and ordered by size, the bodies for which liquid layers are possible are: Rhea, Oberon, Titania, Pluto, Triton, and Europa. Ocean thicknesses range from 16.4 km (Rhea) up to 192.5 km (Triton). All the solutions are purely conductive, and the reduction of the melting temperature is evident in Table 7. As a consequence, convective solutions are not possible because of low temperatures and correspondingly high ice viscosities.

We assume the crystallization of pure water ice and thus, the ammonia concentration within the liquid layer will depend on the ice thickness and on the assumed initial concentration at the time of formation of the satellites. Estimates of the latter for the saturnian system given by Lunine and Stevenson (1987) and Mousis et al. (2002) yield values of about 15 and 1–11.6%, respectively, depending on the N$_2$/NH$_3$ ratio in the saturnian sub-nebula. From observation of comets a abundance of 0.7% was inferred by Bockelée-Morvan et al. (2004). Mea-

Table 7
Heatflow, temperature at the base of the ice shell, and Love numbers obtained from the 3-layer model according to the structure given in Table 6

	Q_s, GW	q_s, mW m^{-2}	T_{bot}, K	k_2	h_2	l_2	X_0, %
Europa	197.6	6.42	263	0.21330	1.0343	0.26953	1.0
	197.6	6.42	259	0.21264	1.0307	0.26830	3.0
	197.6	6.42	253	0.21215	1.0279	0.26745	5.0
	197.6	6.42	242	0.21366	1.0349	0.26982	8.0
	197.6	6.42	215	0.22114	1.0708	0.28155	15.0
Rhea	2.76	3.76	176	0.01293	0.02657	0.00597	0.5
Titania	9.26	1.18	204	0.02933	0.08329	0.01699	1.0
	9.26	1.18	186	0.03369	0.09575	0.01976	3.0
	9.26	1.18	178	0.03629	0.10316	0.02147	4.3
Oberon	7.34	1.01	194	0.02441	0.06596	0.01338	1.0
	7.34	1.01	178	0.02802	0.07576	0.01547	2.9
Triton	69.40	3.02	255	0.16467	0.56018	0.13124	1.0
	69.40	3.02	248	0.16411	0.55827	0.13091	3.0
	69.40	3.02	239	0.16751	0.56992	0.13431	5.0
	69.40	3.02	223	0.17546	0.59720	0.14216	8.0
	69.40	3.02	187	0.19768	0.67341	0.16433	15.0
Pluto	37.75	2.10	252	0.10128	0.30822	0.06721	1.0
	37.75	2.10	240	0.10412	0.31692	0.06957	3.0
	37.75	2.10	226	0.11013	0.33532	0.07442	5.0
	37.75	2.10	175	0.14043	0.42811	0.09959	13.6

Note. The last column shows the assumed initial ammonia content. In this case all the solutions are purely conductive.

surements on the clouds of young stellar objects yield values of only a few percent (Dartois and d'Hendecourt, 2001). Grasset and Pargamin (2005) prefer a value of about 5% in application to Titan. We thus considered initial NH$_3$-abundances of 1, 3, 5, 8, and 15 wt%, respectively.

For the smaller bodies in this study the peritectic composition of 32.5% within the ocean may be reached for a given initial concentration. In that case (all except Europa and Triton) we determined the solution with an initial concentration, leading to a present-day composition close to the peritectic value, but still including a liquid layer. When the peritectic composition is reached, the thermal state of the ocean will be buffered at the peritectic temperature of about 176 K due to the release of latent heat upon water–ammonia crystallization. Since time-dependent solutions are beyond the scope of the present study, we cannot assess on the basis of these models if liquid reservoirs with peritectic composition may have survived up to the present time. In particular, the interiors of small bodies may have entirely solidified over time in the absence of additional internal heat sources because of their larger surface-to-volume ratios. However, for all the bodies considered here, past phases with liquid reservoirs are likely due to the higher radiogenic heat production rates at that time.

For Rhea we obtain a liquid layer only for small initial abundances of ammonia (0.5%). However, if additional internal heat sources were available, peritectic subsurface oceans could also be maintained for higher initial ammonia abundances. Those
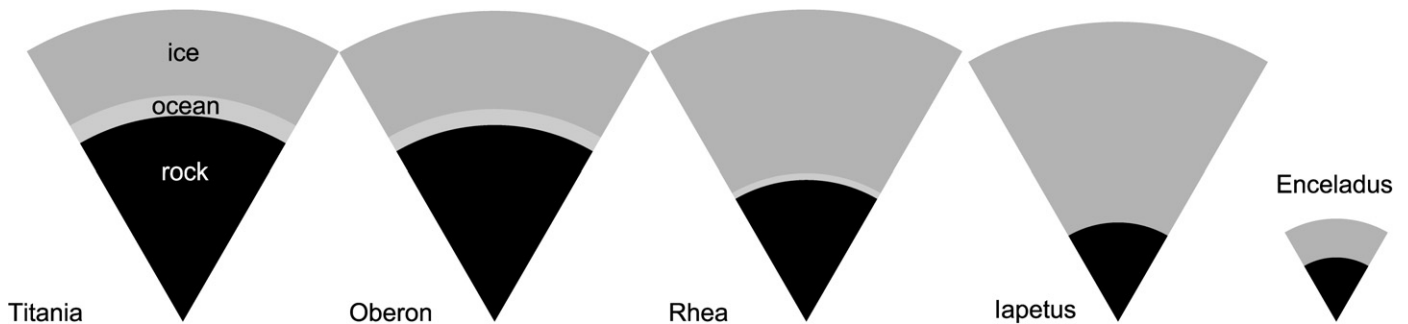

Fig. 6. Examples of interior structures according to the results shown in Tables 3 and 6. For the satellites containing a liquid layer, the models with the following initial NH$_3$-concentrations are shown: Titania, $X_0 = 4.3\%$; Oberon, $X_0 = 2.9\%$, and Rhea, $X_0 = 0.5\%$. The latter values imply present-day liquid layers close to the peritectic composition (see Table 6). Sizes are shown to scale.
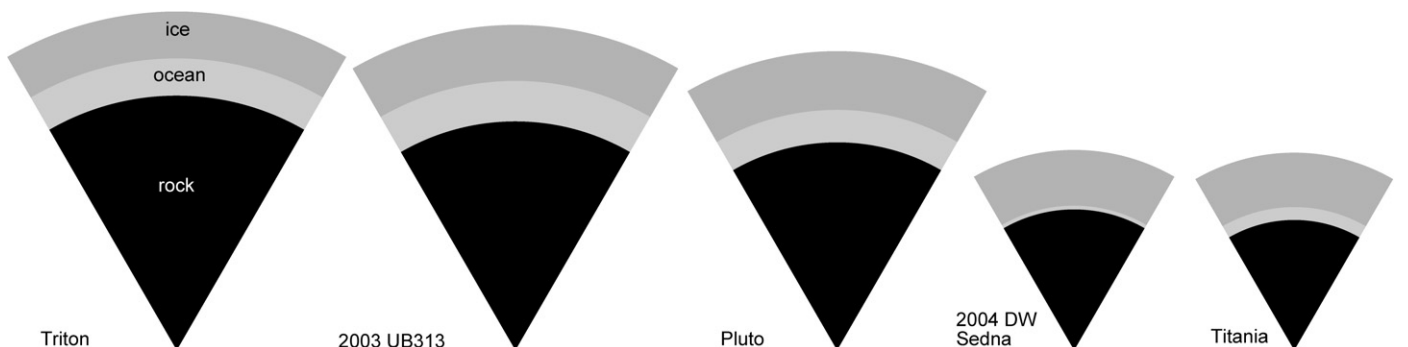

Fig. 7. Interior structure models according to Tables 6 and 8. The following initial NH$_3$-concentrations were used (see Tables 6 and 8): Triton, $X_0 = 5\%$; 2003 UB$_{313}$, $X_0 = 5\%$; Pluto $X_0 = 5\%$; 2004 DW/Sedna, $X_0 = 1.4\%$. Titania is included on the right for size comparison with Fig. 6. Sizes are shown to scale. For UB$_{313}$ we used a radius of 1300 km, which is the lower bound of the value determined by Bertoldi et al. (2006).

Table 8
Results for the largest TNO's (except Pluto and Charon), with an assumed rock-to-H_2O mass ratio of 65%

TNO	R_p, km	M_p, 10^{20} kg	D, km	D_{oc}, km	R_c, km	X, %	X_0, %
2003 UB$_{313}$	≈ 1300	172	242	144	914	3.4	1.0
	≈ 1300	172	224	162	914	14.9	5.0
	≈ 1300	172	179	207	914	21.2	8.0
	≈ 1300	172	169	217	914	31.5	15.0
Sedna/2004 DW	800	40	223	15	562	32.4	1.4

Notes. Shown are the assumed radius (see text for references), the corresponding mass, the thicknesses of the ice layer and the liquid layer, the NH_3-content within the liquid layer X, and the initial NH_3-content X_0, corresponding to X. Identical results are obtained for Sedna and 2004 DW, because their estimated radii are equal. We did not obtain solutions including liquid layers for Quaoar and Ixion or smaller trans-neptunian objects.

oceans would be thicker and the temperature at the bottom of the correspondingly thinner ice shell would be higher due to the pressure dependence of the ammonia–water melting curve. For larger bodies like Europa, Triton, and Pluto, the peritectic composition is not reached even at the present time and for high initial ammonia abundances. The uranian satellites Titania and Oberon range in between these extreme cases. For a moderate initial abundance of a few percent, present-day oceans are obtained for Oberon and Titania as well.

A comparison between models including subsurface oceans and those without internal liquid layers reveals significant differences with respect to the calculated Love numbers. These are found to be about one order of magnitude larger in the presence of subsurface oceans (compare Tables 5 and 7). The outer ice layers are decoupled from the silicate core at depth and can deform more freely so that the corresponding potential variation (Love number k_2) and the radial (h_2) and lateral (l_2) displacements are much larger. This corresponds to results obtained by Sohl et al. (1995) and Moore and Schubert (2000) in application to Titan and Europa, respectively. The dependence of the tidal deformation on the internal structure may be sufficient to indirectly detect subsurface oceans from Love-number measurements from spacecraft, as it is planned for Titan in the course of the *Cassini* mission (Rappaport et al., 1997; Castillo et al., 2002). However, in general the dependence of the tidal response on frequency, viscosity, and rigidity of the ice may introduce some ambiguity in application to the icy satellites (Moore and Schubert, 2000).

3.3. Trans-neptunian objects

The results of Sections 3.1 and 3.2 show that the obtained structures for Triton, Pluto, and Charon are very similar. The mean value of the silicate fraction for Triton, Pluto, and Charon is given by $M_c/M_p = 0.65$. If we assume this value for the trans-neptunian objects (TNO's), it is possible to apply the above models also to these bodies, although their mean densities, or equivalently their masses, are uncertain. We have used a surface temperature of 40 K for all objects. Apart from Pluto and Charon, the largest TNO's known so far are 2003 UB$_{313}$ (Xena) with an estimated radius slightly larger than that of Pluto (Brown et al., 2005; Bertoldi et al., 2006); Sedna

(2003 VB$_{12}$), with an estimated radius of $R_p = 800$ km (Stern, 2005); 2004 DW ($R_p = 800$ km; Fornasier et al., 2004); Quaoar ($R_p = 650$ km; Marchi et al., 2003); and Ixion ($R_p = 550$ km; Marchi et al., 2003). Four of them are even larger than Charon. For 2003 UB$_{313}$ we assumed a radius of 1300 km, which is the lower bound of the value determined by Bertoldi et al. (2006) including the errorbars. Assuming a larger radius, a structure including high-pressure ice phases would also be possible for this object. However, we did not take into account such a possibility in the present study. With the given silicate mass fraction of 0.65, we obtain the masses as shown in Table 8. Results of the model calculations are also shown in Table 8 and in Fig. 7. For the largest object, 2003 UB$_{313}$, a liquid layer would be predicted for all the initial ammonia concentrations considered, with thicknesses ranging from 144 to 217 km. For Sedna and 2004 DW we obtain a liquid layer only for a small initial concentration of $X_0 = 1.4\%$. Higher initial concentrations would result in thicker peritectic subsurface oceans that may have survived if additional heat sources were available. For Sedna and 2004 DW the liquid layer is about 15 km thick located under an ice shell of 223 km thickness. As can be inferred from Fig. 7, the obtained structures of Sedna and 2004 DW are similar to that of Titania. The lower surface temperature leads to a thinner liquid layer for the TNO's. The interior structures of Triton, 2003 UB$_{313}$, and Pluto are also similar (Fig. 7). These bodies have radii around 1000 km, large cores, a relatively high rock content and thick (100–200 km) liquid layers. These bodies belong to the group labeled 'Transition Zone' in Fig. 1 ranging in radius and density between the rocky and mid-sized icy satellites. For the smaller objects, Quaoar and Ixion we did not obtain solutions including liquid layers. According to our model their interior structure will be similar to that of Charon.

4. Discussion and conclusions

We have calculated interior structure models for the medium-sized icy bodies of the outer Solar System assuming thermal equilibrium between radiogenic heat production in the rocky core and the heat loss through the ice shell. Prior to close spacecraft flybys it is not known if these bodies are differentiated, an assumption we used throughout the model. In the jovian system there are, on the one hand, the strongly differentiated satellites Io, Europa, and Ganymede. On the other hand, the internal differentiation of Callisto is likely to be incomplete. Measurements during the Cassini mission will give insight in the internal structures of at least some of the saturnian satellites (Matson et al., 2002). However, there are some aspects, arguing for the internal differentiation of the objects discussed in this study. (1) The surface spectra of the satellites of the outer Solar System are dominated by water ice. Even the TNO Quaoar shows features of crystalline water ice and ammonia hydrate (Jewitt and Luu, 2004), regarded as evidence for recent resurfacing. One possibility would be cryovolcanic activity. Such spectra suggest that at least the outermost region is depleted of silicates thereby implying some degree of differentiation. (2) We included exclusively radiogenic heating of long-lived isotopes as an internal heat source. However, the decay of short-

lived isotopes, like ^{26}Al, may contribute significantly to the heat budget in the early phase of evolution of these bodies. For the largest ones, the generated heat may be sufficient to initiate the process of differentiation (McKinnon, 2002). (3) Tidal heating could have been a relevant heat source in the past for some of the satellites or Kuiper belt binaries. This is most important for satellites which had eccentric orbits in the past, initially or later in their history, for example, due to a resonance crossing. We did not account for such a coupling of the interior heat budget with tidal heating, although it may be important, e.g., for Enceladus, Triton, Pluto, and Charon. In that sense our approach of including only the radiogenic heating of long-lived isotopes can be regarded as a lower bound to internal heating. Other heat sources, if relevant, would make differentiation and also the formation of liquid layers even more likely. However, the internal differentiation of these bodies is an assumption which has to be confirmed or disproved by future spacecraft measurements.

Including initial ammonia abundances based on most recent observational evidence, we obtain subsurface oceans even at the present time for Europa, Rhea, Titania, Oberon, Triton, Pluto, and the TNO's 2003 UB$_{313}$, Sedna and 2004 DW. For the larger bodies (Europa, Triton, Pluto, and 2003 UB$_{313}$) we obtain solutions including an internal ocean even in the whole range of initial ammonia concentration from 1 to 15%. For the smaller bodies we obtain subsurface oceans only for initial ammonia concentrations of a few percent. Higher initial ammonia abundances would require additional internal heat sources to maintain thicker, peritectic subsurface oceans. Note, that our model is not applicable to the large icy satellites Ganymede, Callisto, and Titan because we did not include the formation of high-pressure ice phases. For the latter liquid water–ammonia layers are also expected on the basis of thermal modeling (Grasset et al., 2000; Spohn and Schubert, 2003; Sohl et al., 2003). The pressures inside the H$_2$O layer of the satellites discussed in this study are small, and high pressure ice layers do not form. However, the ice shells of the large bodies with relatively thick H$_2$O layers, i.e., Triton, Pluto, and 2003 UB$_{313}$, have basal pressures that are sufficient for pressure-induced phase transitions to occur. Some examples of the obtained internal structures are shown in Figs. 6 and 7.

For the bodies discussed here, the liquid layers are in direct contact with the rocky cores. This contrasts with subsurface oceans inside the large icy satellites like Ganymede, Callisto, or Titan, where they are enclosed between ice-I at the top and high-pressure ice layers at the bottom. The silicate–water contact would allow the highly efficient exchange of minerals and salts between the rocks and the ocean in the interiors of those medium-sized satellites.

Subsurface oceans should have an influence on the interaction of the satellite with the magnetosphere of their planets. If there are ions contained in the liquid, and if the water layer surrounds the whole satellite, which is expected according to this study, secondary fields should exist, due to the time-varying magnetic field of the primary felt by the satellite. There may be the chance during the *Cassini* mission to search for these signals on the occasion of close flybys at the satellites. Targets of special interest in the saturnian system are Rhea and

also Iapetus, which is with the given uncertainties of the model parameters at least close to possessing a subsurface ocean. According to this study, we would not expect present-day liquid layers on Mimas, Enceladus, Dione, and Tethys in the absence of heat sources other than radiogenic heating. Note, however, that it is very likely that Titan possesses an internal water–ammonia ocean under these circumstances (Grasset et al., 2000; Sohl et al., 2003; Tobie et al., 2005).

Another way to detect subsurface oceans from spacecraft is to determine the Love numbers from measurements of the tidal deformation of the satellites. The Love numbers are about one order of magnitude larger in the presence of an internal ocean. In that case the ice shell is decoupled from the rocky core and can move freely above the liquid layer. Consequently, tidal deformations of the ice shell are much stronger. Such an experiment is planned for the *Cassini* mission during several dedicated flybys at Titan. However, tidal Love number determinations at Rhea and Iapetus would also be useful to prove or disprove the existence of possible subsurface oceans inside these moons.

There may be a relation between the presence of an internal ocean and geological features visible at the satellites' surfaces. However, this will depend on the thickness of the ice layer above the ocean; e.g., in case of Rhea, the liquid layer is relatively thin (≈ 16 km) and lies underneath a thick (≈ 400 km) ice shell. Therefore, it is questionable if the internal ocean would have an influence on the surface. The example of the heavily cratered surface of Callisto suggests that the existence of a subsurface ocean, evident from measured induction signals (Khurana et al., 1998; Zimmer et al., 2000) and thermal modeling (Spohn and Schubert, 2003), does not necessarily imply geologic activity and surface alteration. In case of Callisto the ice layer is expected to be about 80 km thick. Therefore, the presence of an internal ocean on Rhea would not be in conflict with the satellite's heavily cratered surface.

Our model does not give an explanation for the present geologic and endogenic activity of Enceladus (Porco et al., 2006; Spencer et al., 2006). If there ever existed an ocean inside Enceladus, heat sources other than radiogenic heating would be required. One option would be tidal heating. Assuming the eutectic temperature of 176 K as a minimum temperature for a possible subsurface ocean, the required heat source would be about 11 times the value of radiogenic heating alone. To provide such a high value by tidal heating is difficult to achieve. The most relevant parameters for the tidal heating rate are the orbital eccentricity and the viscosity in the interior. The eccentricity of 0.0044 of Enceladus is forced by the 2:1 mean motion resonance with Dione. As pointed out by Peale (1999) the evolution into resonance can occur very smoothly, without the occurrence of high eccentricity values due to any chaotic behavior in the history of the satellite. In this case the eccentricity of Enceladus should have been even lower in the past. In such a scenario, we are only left with the possibility to enhance the tidal heating rate by artificially lowering the viscosity of the interior, especially in the ice layer. As an extreme assumption, we may consider a vigorously convecting low-viscosity ice layer surrounded by a viscous veneer layer of one kilometer thick-

ness at surface temperature. The required heating rate could be attained only if the viscosity of the ice layer were of the order of 10^{13} Pa s, i.e., close to the melting point viscosity of water ice. Such a low value of the viscosity is unrealistic, however, if the temperature at the base of the shell equals the minimum melting temperature of 176 K, which is at least required for an internal water–ammonia ocean to form. For a pure water layer the situation would even be worse, because in that case temperatures of about 270 K would have to be reached in the ice layer. It should be noted that any hypothesis of ocean formation on Enceladus due to internal processes must also explain the difference to Mimas, which is similar in bulk composition but closer to Saturn, thereby implying even stronger tidal forces. As also noted by Peale (1999), a thorough investigation of the phase-space of the Enceladus–Dione resonance using modern nonlinear dynamics has not yet been performed. It may turn out, that the orbital history of Enceladus is not as simple as originally thought (see also Callegari and Yokoyama, 2005). We favor such a possibility, because an increase of eccentricity would significantly enhance the tidal dissipation rate without the need of invoking extreme rheological assumptions. However, we did not yet investigate such a scenario and note, that the history of Enceladus must be different from those of the other satellites. This also applies to the uranian Satellite Miranda. Our model does not help explain the satellite's remarkable surface features. Here again other scenarios are required, which are not subject of this study. To summarize this aspect, it is suggested that there is a link between internal oceans and surface features only if the ice layers are relatively thin (up to a few tens of kilometers) which may be the case for Europa and also for Triton and Pluto at the beginning of their evolutions. Apart from Europa we obtain ice layer thicknesses of more than 140 km making a direct link between subsurface oceans and surface geology unlikely. However, ice thicknesses are expected to be smaller in the past due to the higher radiogenic heating rate. If we enhance the heating rate in the case of Rhea by a factor of 10, which roughly corresponds to the heating rate at the beginning of the Solar System, and assume a high initial ammonia abundance of 15%, which leads to a solution with maximum ocean thickness, we still obtain an ice layer of more than 100 km thickness. The situation is different on Triton for which we obtain an ice thickness of 22 km for $X_0 = 15\%$ and a 10 times larger heating rate. Therefore the possibility of thin ice layers in the past is given, at least for the larger bodies. Therefore it will be worthwhile to calculate evolution models, which will be addressed in future work.

The fact that the liquid layers crystallize during the satellites' histories may have interesting consequences which are not discussed in detail here. First, there will be an increase in volume of the ice layer when it is transformed from the liquid into the solid state, because ice-I is less dense than water. As a consequence, this may lead to the early formation of extensional features at the surface of icy satellites (Nimmo, 2004). Second, we have shown that the Love numbers decrease significantly when the internal ocean solidifies and the icy layer is no longer mechanically decoupled from the rocky core underneath. Therefore, tidal dissipation rates also decrease significantly at a certain point in the satellite's evolution, when the liquid layer is

completely solidified. This would have consequences for the orbital evolution of the satellites. In general, the satellites slowly drift outward from their primaries due to the tidal torque exerted on them. However, this process is slowed down if there is substantial tidal dissipation within the satellite. At the point where the subsurface ocean freezes completely, the dissipation rate in the satellite decreases abruptly so that the satellite will drift outward at a faster rate. This may have consequences for satellites orbiting close to their parent bodies, for which tidal interactions are stronger. Additionally, the influence on resonance capture, e.g., in the case of Dione being in resonance with Enceladus, has to be investigated.

As summarized in Table 3 we have obtained possible two-layer solutions for all satellites except Triton. These models were calculated for pure water ice layers. For some of the satellites we also obtained three-layer structures including a liquid layer. Which state (two- or three-layer) is actually obtained by a satellite depends on the volatile (ammonia) content and also on the temperature shortly after accretion. At that time the satellites were heated substantially not only due to long-lived radioactive isotopes but also maybe due to the decay of short-lived radioactives like ^{26}Al and the conversion of potential energy into heat during the differentiation process. Therefore, our models underestimate the heat sources at least at early stages of a satellite's evolution. Taking this into account and assuming that there is a small amount of ammonia present, the oceans are likely to have formed shortly after differentiation. For the largest bodies the liquid layers could still exist at present.

In general, we argue that internal oceans may be a common phenomenon (at least in the past) of the satellites of the outer Solar System and other icy bodies like the large trans-neptunian objects. The consequences of subsurface oceans are important for these planetary bodies with respect to orbital evolution, internal dynamics, and astrobiological implications. However, more observations are required to confirm or disprove their existence which can be provided by the search for induced magnetic fields and the determination of tidal Love numbers during the *Cassini* mission in case of the saturnian satellites and by future space missions targeted to other outer Solar System bodies.

Acknowledgments

References

Anderson, J.D., Schubert, G., Jacobson, R.A., Lau, E.L., Moore, W.B., Sjogren, W.L., 1998. Europa's differentiated internal structure: Inferences from four Galileo encounters. Science 281, 709–712.

Bertoldi, F., Altenhoff, W., Weiss, A., Menten, K.M., Thun, C., 2006. The trans-neptunian object UB$_{313}$ is larger than Pluto. Nature 439, 563–564.

Bockelée-Morvan, D., Crovisier, J., Mumma, M.J., Weaver, H.A., 2004. The composition of cometary volatiles. In: Festou, M.C., Keller, H.U., Weaver, H.A. (Eds.), Comets II. Univ. of Arizona Press, Tucson, pp. 391–423.

Brown, M.E., Trujillo, C.A., Rabinowitz, D.L., 2005. Discovery of a planetary-sized object in the scattered Kuiper belt. Astron. J. 635, 97–100.

Callegari Jr., N., Yokoyama, T., 2005. Dynamics of 2 satellites in the 2/1 mean-motion resonance. In: ACM Meeting 2005. Abstract P10.2.

Castillo, J., Rappaport, N., Mocquet, A., Sotin, C., 2002. Clues on Titan's internal structure from Cassini–Huygens Mission. In: 33rd Annual LPSC 2002, Houston, Texas. Abstract 1989.

Chizhov, V.E., 1993. Thermodynamic properties and thermal equations of state of high-pressure ice phases. Prikl. Mekh. Tekh. Fiz. Engl. Transl. 2, 113–123.

Dartois, E., d'Hendecourt, L., 2001. Search for ammonia ice in cold dust envelopes around YSOs. Astron. Astrophys. 365, 144–165.

Davaille, A., Jaupart, C., 1993. Transient high-Rayleigh-number thermal convection with large viscosity variations. J. Fluid Mech. 253, 141–166.

Deschamps, F., Sotin, C., 2001. Thermal convection in the outer shells of large icy satellites. J. Geophys. Res. 106, 5107–5121.

Durham, W.B., Stern, L.A., 2001. Rheological properties of water ice—Applications to satellites of the outer planets. Annu. Rev. Earth Planet. Sci. 29, 295–330.

Durham, W.B., Kirby, S.H., Stern, L.A., 1998. Rheology of planetary ices. In: Schmitt, B., de Bergh, C., Festou, M. (Eds.), Solar System Ices. Kluwer Academic, Dordrecht, pp. 63–78.

England, C., 2003. Are there oceans under the ice of small saturnian and uranian moons? Bull. Am. Astron. Soc. 35 (4). DPS meeting abstract 15.02.

Fornasier, S., Dotto, E., Barucci, M.A., Barbieri, C., 2004. Water ice on the surface of the large TNO 2004 DW. Astron. Astrophys. 422, 43–46.

Gillies, G.T., 1990. Resource Letter MNG-1: Measurements of Newtonian Gravitation. Am. J. Phys. 58, 525–534.

Grasset, O., Pargamin, J., 2005. The ammonia–water system at high pressures: Implications for the methane of Titan. Planet. Space Sci. 53, 371–384.

Grasset, O., Parmentier, E.M., 1998. Thermal convection in a volumetrically heated, infinite Prandtl number fluid with strongly temperature-dependent viscosity Implications for planetary evolution. J. Geophys. Res. 103, 18171–18181.

Grasset, O., Sotin, C., Deschamps, F., 2000. On the internal structure and dynamics of Titan. Planet. Space Sci. 48, 617–636.

Hunten, D.M., Tomasko, M.G., Flasar, F.M., Samuelson, R.E., Strobel, D.F., Stevenson, D.J., 1984. Titan. In: Gehrels, T., Matthews, M.S. (Eds.), Saturn. Univ. of Arizona Press, Tucson, pp. 671–759.

Jacobson, R.A., Riedel, J.E., Taylor, A.H., 1991. The orbits of Triton and Nereid from spacecraft and Earthbased observations. Astron. Astrophys. 247, 565–575.

Jacobson, R.A., Campbell, J.K., Taylor, A.H., Synnott, S.P., 1992. The masses of Uranus and its major satellites from Voyager tracking data and Earth-based uranian satellite data. Astron. J. 103, 2068–2078.

Jacobson, R.A., Antreasian, P.G., Bordi, J.J., Criddle, K.E., Ionasescu, R., Jones, J.B., Mackenzie, R.A., Pelletier, F.J., Owen Jr., W.M., Roth, D.C., Stauch, J.R., 2005. The gravity field of the saturnian system and the orbits of the major saturnian satellites. Bull. Am. Astron. Soc. 37, 729.

Jewitt, D.C., Luu, J., 2004. Crystalline water ice on the Kuiper belt object (50000) Quaoar. Nature 432, 731–733.

Khurana, K.K., Kivelson, M.G., Stevenson, D.J., Schubert, G., Russell, C.T., Walker, R.J., Polanskey, C., 1998. Induced magnetic fields as evidence for subsurface oceans in Europa and Callisto. Nature 395, 777–780.

Kirk, R.L., Stevenson, D.J., 1987. Thermal evolution of a differentiated Ganymede and implications for surface features. Icarus 69, 91–134.

Kivelson, M.G., Khurana, K.K., Russell, C.T., Volwerk, M., Walker, R.J., Zimmer, C., 2000. Galileo magnetometer measurements: A stronger case for a subsurface ocean at Europa. Science 289, 1340–1343.

Kivelson, M.G., Khurana, K.K., Volwerk, M., 2002. The permanent and inductive magnetic moments of Ganymede. Icarus 157, 507–522.

Leliwa-Kopystyński, J., Maruyama, M., Nakajima, T., 2002. The water–ammonia phase diagram up to 300 MPa: Application to icy satellites. Icarus 159, 518–528.

Lewis, J.S., 1971. Satellites of the outer planets: Their physical and chemical nature. Icarus 15, 174–185.

Lunine, J.I., Stevenson, D.J., 1987. Clathrate and ammonia hydrates at high pressure-application to the origin of methane on Titan. Icarus 70, 61–77.

Marchi, S., Lazzarin, M., Magrin, S., Barbieri, C., 2003. Visible spectroscopy of the two largest known trans-neptunian objects: Ixion and Quaoar. Astron. Astrophys. 408, L17–L19.

Matson, D.L., Spilker, L.J., Lebreton, J.-P., 2002. The Cassini/Huygens Mission to the saturnian system. Space Sci. Rev. 104, 1–58.

McKinnon, W.B., 1998. Geodynamics of icy satellites. In: Schmitt, B., de Bergh, C., Festou, M. (Eds.), Solar System Ices. Kluwer Academic, Dordrecht, pp. 525–550.

McKinnon, W.B., 2002. On the initial thermal evolution of Kuiper belt objects. In: Warmbein, B. (Ed.), Proceedings of Asteroids, Comets, Meteors—ACM, 2002, ESA SP-500. ESA Publications Division, Noordwijk, ISBN 92-9092-810-7, pp. 29–38.

Moore, W.B., Schubert, G., 2000. The tidal response of Europa. Icarus 147, 317–319.

Mousis, O., Gautier, D., Bockelée-Morvan, D., 2002. An evolutionary turbulent model of the Saturn's subnebula implications on the origin of the atmosphere of Titan. Icarus 156, 162–175.

Multhaup, K., Spohn, T., 2005. Stagnant lid convection in the mid-sized icy satellites of Saturn. Icarus. Submitted for publication.

Nimmo, F., 2004. Stresses generated in cooling viscoelastic ice shells: Application to Europa. J. Geophys. Res. 109, doi:10.1029/2004JE002347. 12001.

Null, G.W., Owen, W.M., 1996. Charon/Pluto mass ratio obtained with HST CCD observations in 1991 and 1993. Astron. J. 111, 1368–1381.

Peale, S.J., 1999. Origin and evolution of the natural satellites. Annu. Rev. Astron. Astrophys. 37, 533–602.

Porco, C.C., and 24 colleagues, 2006. Cassini observes the active south pole of Enceladus. Science 311, 1393–1401.

Rainey, E.S., Stevenson, D.J., 2003. Oceans in ice-rock bodies: Conditions for the existence of subsurface liquid water. Eos. Trans. Amer. Geophys. Union 84 (46). Fall Meet. Suppl. Abstract P51B-0447.

Rappaport, N., Bertotti, B., Giampieri, G., Anderson, J.D., 1997. Doppler measurements of the quadrupole moments of Titan. Icarus 126, 313–323.

Schubert, G., Cassen, P., Young, R.E., 1979. Subsolidus convective cooling histories of terrestrial planets. Icarus 38, 192–211.

Schubert, G., Spohn, T., Reynolds, R.T., 1986. Thermal histories, compositions and internal structures of the moons of the Solar System. In: Burns, J.A., Matthews, M.S. (Eds.), Satellites. Univ. of Arizona Press, Tucson, pp. 224–292.

Schubert, G., Turcotte, D.L., Olson, P., 2001. Mantle Convection in the Earth and Planets. Cambridge Univ. Press, Cambridge, UK.

Schubert, G., Anderson, J.D., Spohn, T., McKinnon, W.B., 2004. Interior composition, structure and dynamics of the Galilean satellites. In: Bagenal, F., Dowling, T.E., McKinnon, W.B. (Eds.), Jupiter. The Planet, Satellites and Magnetosphere. Cambridge Univ. Press, Cambridge, UK, pp. 281–306.

Segatz, M., Spohn, T., Ross, M.N., Schubert, G., 1988. Tidal dissipation, surface heat flow and figures of viscoelastic models of Io. Icarus 75, 187–206.

Seidelmann, P.K., Abalakin, V.K., Bursa, M., Davies, M.E., de Bergh, C., Lieske, J.H., Oberst, J., Simon, J.L., Standish, E.M., Stooke, P., Thomas, P.C., 2002. Report of the IAU/IAG working group on cartographic coordinates and rotational elements of the planets and satellites: 2000. Celest. Mech. Dynam. Astron. 82, 83–111.

Sicardy, B., and 44 colleagues, O., 2006. Charon's size and an upper limit on its atmosphere from a stellar occultation. Nature 439, 52–54.

Sohl, F., Sears, W.D., Lorenz, R.D., 1995. Tidal dissipation on Titan. Icarus 115, 278–294.

Sohl, F., Spohn, T., Breuer, D., Nagel, K., 2002. Implications from Galileo observations on the interior structure and chemistry of the Galilean satellites. Icarus 157, 104–119.

Sohl, F., Hussmann, H., Schwentker, B., Spohn, T., Lorenz, R.D., 2003. Interior structure models and Love numbers of Titan. J. Geophys. Res. 108 (E12), doi:10.1029/2003JE002044. 5130.

Solomatov, V.S., 1995. Scaling of temperature- and stress-dependent viscosity convection. Phys. Fluids 7, 266–274.

Sotin, C., Grasset, O., Beauchesne, S., 1998. Thermodynamic properties of high-pressure ices: Implications for the dynamics and internal structure of large icy satellites. In: Schmitt, B., de Bergh, C., Festou, M. (Eds.), Solar System Ices. Kluwer Academic, Norwell, MA, pp. 79–96.

Spencer, J.R., Pearl, J.C., Segura, M., Flasar, F.M., Mamoutkine, A., Romani, P., Buratti, B.J., Hendrix, A.R., Spilker, L.J., Lopes, R.M.C., 2006. Cassini

encounters Enceladus: Background and the discovery of a south polar hot spot. Science 311, 1401–1405.

Spohn, T., Schubert, G., 2003. Oceans in the icy Galilean satellites of Jupiter? Icarus 161, 456–467.

Stern, S.A., 2005. Regarding the accretion of 2003 VB$_{12}$ (Sedna) and like bodies in distant heliocentric orbits. Astron. J. 129, 526–529.

Thomas, P.C., 1988. Radii, shapes, and topography of the satellites of Uranus from limb coordinates. Icarus 73, 427–441.

Thomas, P.C., 2000. The shape of Triton from Limb profiles. Icarus 148, 587–588.

Tobie, G., Grasset, O., Lunine, J.I., Mocquet, A., Sotin, C., 2005. Titan's internal structure inferred from a coupled thermal-orbital model. Icarus 175, 496–502.

Turcotte, D.L., Schubert, G., 2001. Geodynamics, second ed. Cambridge Univ. Press, Cambridge, UK.

Weertman, J., 1983. Creep deformation of ice. Annu. Rev. Earth Planet. Sci. 11, 215–240.

Wieczerkowski, K., 1999. Gravito-Viskoelastodynamik für verallgemeinerte Rheologien mit Anwendungen auf den Jupitermond Io und die Erde. Ph.D. thesis. Dtsch. Geod. Komm., Reihe C, 515, Munich, Germany.

Yoder, C.F., 1995. Astrometric and geodetic properties of Earth and the Solar System. In: Ahrens, T. (Ed.), Global Earth Physics. A Handbook of Physical Constants. American Geophysical Union, Washington, DC, pp. 1–31.

Zimmer, C., Khurana, K.K., Kivelson, M.G., 2000. Subsurface oceans on Europa and Callisto: Constraints from Galileo magnetometer observations. Icarus 147, 329–347.

Zschau, J., 1978. Tidal friction in the solid Earth: Loading tides versus body tides. In: Brosche, P., Sündermann, J. (Eds.), Tidal Friction and the Earth's Rotation. Springer, New York, pp. 62–94.